

Towards a complete census of luminous Compton-thick Active Galactic Nuclei in the local Universe

A. Akylas¹, I. Georgantopoulos¹, P. Gandhi², P. Boorman³, and C. L. Greenwell⁴

¹ Institute for Astronomy Astrophysics Space Applications and Remote Sensing (IAASARS), National Observatory of Athens, Ioannou Metaxa & Vasileos Pavlou, Penteli, 15236, Greece

² School of Physics and Astronomy, University of Southampton, Highfield, Southampton, SO17 1BJ, United Kingdom

³ Cahill Center for Astrophysics, California Institute of Technology, 1216 East California Boulevard, Pasadena, CA 91125, USA

⁴ Physics Department, University of Durham, South Road, DH1 3LE, United Kingdom

October 1, 2024

ABSTRACT

X-ray surveys provide the most efficient means for the detection of Active Galactic Nuclei (AGN). However, they face difficulties in detecting the most heavily obscured Compton-thick AGN. The BAT detector on board the *Gehrels/Swift* mission, operating in the very hard 14-195 keV band, has provided the largest samples of Compton-thick AGN in the local Universe. However, even these flux limited samples can miss the most obscured sources among the Compton-thick AGN population. A robust way to find these local sources is to systematically study volume-limited AGN samples detected in the IR or the optical part of the spectrum. Here, we utilize a local sample (<100 Mpc) of mid-IR selected AGN, unbiased against obscuration, to determine the fraction of Compton-thick sources in the local universe. When available we acquire X-ray spectral information for the sources in our sample from previously published studies. Additionally, to maximize the X-ray spectral information for the sources in our sample, we analyse, for the first time, eleven unexplored *XMM-Newton* and *NuSTAR* observations, identifying four new Compton-thick sources. Our results reveal an increased fraction of Compton-thick AGN among the sources that have not been detected by BAT of 44 %. Overall we estimate a fraction of Compton thick sources in the local universe of 25-30% among mid-IR selected AGN. We find no evidence for evolution of the AGN Compton-thick fraction with luminosity.

Key words. X-rays: general – galaxies: active – quasars: supermassive black holes

1. Introduction

X-ray emission is ubiquitous in Active Galactic Nuclei (AGN). This is believed to originate from a corona above the accretion disk (e.g. Haardt & Maraschi 1991). According to this picture, the UV photons produced in the accretion disk are scattered by the hot coronal electrons having temperatures of about 60 keV (Akylas & Georgantopoulos 2021) producing copious amounts of X-ray emission. The X-ray radiation that permeates the sky, the X-ray background Giacconi et al. (1962), in the energy range 0.1-300 keV is produced by the superposition of AGN. The *Chandra* X-ray mission owing to its superb spatial resolution resolved about 90% of the X-ray background in the relatively soft 0.5-8 keV band (Mushotzky et al. 2000). Indeed, optical spectroscopic observations confirm that the vast majority of these sources are associated with AGN with redshifts peaking at $z \approx 0.7$ (e.g. Luo et al. 2017).

Observations with the *Gehrels/Swift* /BAT (Ajello et al. 2008), *RXTE* (Revnivtsev et al. 2003), *BeppoSAX* (Frontera et al. 2007), *Integral* (Churazov et al. 2007) missions show that the peak energy density of the X-ray background lies at harder energies around 30 keV. The X-ray background synthesis models attempt to reproduce the spectrum of the X-ray background by modeling the AGN luminosity function together with their spectral properties (Comastri et al. 1995; Gilli et al. 2007; Treister

et al. 2009; Akylas et al. 2012; Ueda et al. 2014; Ananna et al. 2019). All X-ray background models find that in order to reproduce the 30 keV energy hump one needs a considerable fraction of heavily obscured Compton-thick AGN. However, the exact fraction depends on the amount of reflection in the vicinity of the emitted radiation that is the accretion disk and the surrounding torus (Gandhi et al. 2007; Vasudevan et al. 2013). In Compton-thick sources, the line-of-sight to the nucleus is obscured by huge amounts of gas with column densities exceeding $N_{\text{H}} \approx 10^{24} \text{ cm}^{-2}$. The obscuring screen is believed to be a dusty structure with toroidal geometry. Recent observations suggest that this obscuring screen, the torus, is composed of optically thick clouds Nenkova et al. (2002, 2008); Tristram et al. (2007). In Compton-thick AGN the obscuration is because of Compton-scattering rather than photoelectric absorption. The X-ray photons below 10 keV are almost totally absorbed and hence X-ray observations at higher energies are necessary in order to securely classify a source as a Compton-thick AGN. The exact fraction of Compton-thick sources among the total AGN population differs significantly among the various X-ray background models. Akylas et al. (2012) estimate a rather modest fraction of less than about 20%, see also Treister et al. (2009); Vasudevan et al. (2013). On the other end the models of Ananna et al.

(2019) find that the Compton-thick AGN could constitute half of the AGN population.

The launch of the *Gehrels/Swift* mission Gehrels et al. (2004) made a leap forward in the study of Compton-thick AGN owing to its hard energy range. The Burst Alert Telescope, BAT, onboard *Gehrels/Swift* continuously scans the whole sky in the 14-195 keV band. Therefore, BAT provided an unprecedented census of the hard X-ray sky and in particular of Compton-thick AGN. Ricci et al. (2015), Akylas et al. (2016) analysed the AGN X-ray spectra in the BAT 70-month survey (Baumgartner et al. 2013) finding a few tens of candidate Compton-thick AGN. In addition, Marchesi et al. (2018), Zhao et al. (2021), Torres-Albà et al. (2021) searched for Compton-thick AGN on the Palermo 100-month BAT catalogue. Using the BAT sample Akylas et al. (2016) and recently Ananna et al. (2022) derived for the first time the Compton-thick AGN luminosity function in the local Universe. More recently Georgantopoulos et al. (submitted) revisit these luminosity functions using the most up-to-date column density estimates derived by *NuSTAR*. According to the above works, the fraction of Compton-thick AGN should not exceed 25% of the total AGN population (see also Burlon et al. 2011; Ricci et al. 2015; Georgantopoulos & Akylas 2019; Torres-Albà et al. 2021).

Nevertheless, the Compton-thick AGN detected by BAT may be the tip of the iceberg. This is because even the BAT band (14-195 keV) may miss a significant fraction of heavily obscured AGN. Burlon et al. (2011) finds that even mildly Compton-thick AGN, with a column density of a few times 10^{24}cm^{-2} , are attenuated by 50% in the hard 15-55 keV band. The most heavily obscured, reflection dominated Compton-thick AGN with column densities $N_{\text{H}} \approx 10^{25}\text{cm}^{-2}$ such as NGC 1068 have the bulk of their 15-55 keV flux attenuated. In order to find the most heavily obscured AGN one has to resort to volume-limited optically selected or IR selected AGN. Along these lines, Akylas & Georgantopoulos (2009) observed with *XMM-Newton* all (38) Seyfert-2 galaxies in the Palomar spectroscopic sample of galaxies (Ho et al. 1997). They find that the fraction of Compton-thick sources among Seyfert-2 galaxies is about 20%. Recently, Asmus et al. (2020) compiled the most complete so far galaxy sample in the local Universe ($< 100\text{Mpc}$). They select AGN applying the selection criteria based on the *WISE* W1-W2 colour (Assef et al. 2018). This sample comprises of about 150 sources and has been routinely observed by most X-ray missions. For these sources, we compile the already published results and we analyse for the first time the X-ray spectra of eleven sources. Our goal is to provide the most definitive yet estimate of the fraction of Compton-thick sources among the *WISE* selected AGN in the local Universe.

Our paper is organised as follows. In section 2 we describe in detail the sample of Asmus et al. (2020) and the selection criteria applied. In section 3 we detail the new X-ray observations obtained by *NuSTAR*, *XMM-Newton* and *Chandra*. The spectral fit results are presented in Section 4. The discussion and the summary are presented in sections 5 and 6 respectively.

2. The sample

In this work we utilize data from the Local AGN survey (LASr) sample, (Asmus et al. 2020), which provides the most complete census of mid-IR selected AGN among all galaxies within a volume of 100 Mpc. The sample contains 49k galaxies and has a completeness of 90% at $\log M_{\star}/M_{\odot} = 9.4$. Then, the applied *WISE* identification criteria serve as a robust tracer of AGN emission. Briefly, the sources selected satisfy the following criteria:

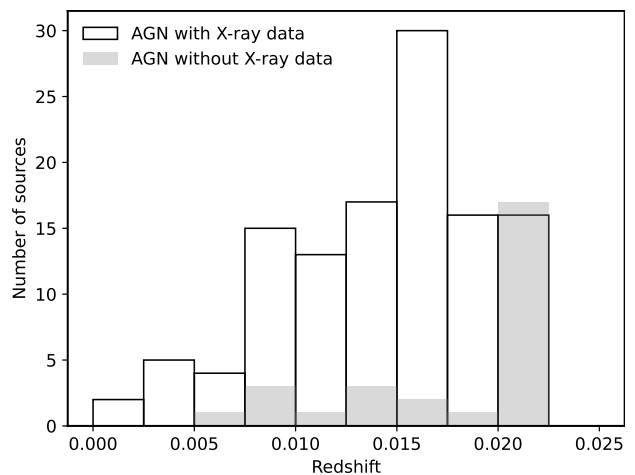


Fig. 1. The redshift distribution of the sources in the "known AGN" sample. The solid line histogram represents the distribution of sources with available X-ray data and the gray shaded histogram the distribution of the sources without X-ray data.

(a) the W1 ($3.4\mu\text{m}$), W2 ($4.6\mu\text{m}$) AGN selection criterion from (Assef et al. 2018). This criterion is based on the hot emission coming from the AGN heated obscuring torus, becoming prominent at short mid-IR wavelengths ($< 50\mu\text{m}$). (b) the theoretical colour criterion based on the *WISE* W2 and W3 ($12\mu\text{m}$) presented in Satyapal et al. (2018), to separate AGN from luminous starbursts and (c) $L(12\mu\text{m}) > 10^{42.3}\text{erg s}^{-1}$. According to Asmus et al. (2020), the above criteria ensure a reliability of over 90% for finding an AGN.

Consequently, the above authors derive two AGN datasets. The first, is the "known AGN" sample containing *WISE* selected AGN, already known to host an active nucleus in the literature. The second, the "new AGN" sample, contains the *WISE* selected AGN which have no prior AGN classification in the literature.

In this study, we primarily focus on the "known AGN" sample. This is because the "new AGN" sample has practically no X-ray information available. On the other hand, as anticipated, the "known AGN" sample contains a large fraction of sources (approximately 75%) detected within *XMM-Newton*, *NuSTAR* or BAT observations. The remaining sources (about 25%) are not present in the above archives and lack usable X-ray data. Among the remaining sources, less than 30% fall within the footprint of *Gehrels/Swift* /XRT observations, and even fewer cases allow for the extraction of a poor quality X-ray spectrum.

In Fig. 1 we compare the redshift distribution of the sources within these two sub-samples. Notably, the majority of the sources lacking X-ray data are concentrated in the highest redshift bin, i.e. between 0.02 and 0.022. At lower redshift values the fraction of the sources without X-ray data is very small. Based on this plot and in order to improve the X-ray completeness of our sample, we apply a cut at the redshift of $z=0.02$ ($\sim 87\text{Mpc}$).

After applying all the selection criteria to the optically selected, "known AGN sample", we have identified 113 AGN. Among these, the largest number (72 sources) have also been detected in the 70-month *Swift*/BAT all-sky survey (Baumgartner et al. 2013). Their X-ray spectral properties have been systematically studied in detail in Ricci et al. (2017) primarily using *XMM-Newton* and *Gehrels/Swift* /BAT spectra. Additionally, several individual studies re-analysed specific cases, particularly

those considered as Compton-thick candidates, utilizing also *NuSTAR* observations.

Among the 41 sources that have not been detected by BAT, 14 have already been analysed using archival *NuSTAR* and/or *XMM-Newton* observations and their results have been presented in the literature. Additionally a search within the *NuSTAR* and *XMM-Newton* archives yields good quality X-ray data for eleven additional sources which have not been reported in the literature. For the remaining sources, those lacking *NuSTAR* *XMM-Newton* or BAT observations, we query the *Gehrels/swift* X-ray Telescope (XRT) Science Data Centre repository (Evans et al. 2009) to obtain spectral fits, when possible. The cross correlation with the XRT 2SXPS catalogue (Evans et al. 2020) reveals five sources with spectral information available. Thus only eleven sources (i.e less than 10%) of our sample remains without X-ray spectral information. After the above selections our working sample with available X-ray observation is composed of 102 sources (see Table 1.) For the sake of completeness we mention that there are 32 sources in the "new AGN" sample following the same mid-IR selection criteria, up to a redshift of $z=0.02$.

In Table A.1 we present the list of our sources. The X-ray spectral information is obtained from either from the literature or from our own spectral analysis. A detailed discussion of the newly analyzed sources is presented in sections 3 and 4.

3. New X-ray observations

In Table 2 we present the X-ray log of the eleven sources with available archival *XMM-Newton* or *NuSTAR* X-ray data, which are presented for the first time in this work. In particular, five sources have both *NuSTAR* and *XMM-Newton* data, one source presents only *NuSTAR* and *Chandra* data while five sources have only *XMM-Newton* observations available.

In the table there is an additional entry, i.e. the case of IC4995. Recently, Osorio-Clavijo et al. (2022) reported IC4995 as a Compton-thick AGN using the same *NuSTAR* data set presented here. However, their analysis employed a rather simple model. Given the Compton-thick nature of this source, we chose to re-analyze the same *NuSTAR* data in conjunction with *XMM-Newton* observations to derive more accurate estimations for its luminosity and column density.

In the case of the five sources in our sample with *Gehrels/Swift* /XRT data, marked with an *s* in Table A.1, we have not performed the X-ray data reduction or analysis. The X-ray spectral data has been retrieved from the *Gehrels/Swift* /XRT Science Data Centre repository (Evans et al. 2020).

3.1. *XMM-Newton* data reduction

We restrict our analysis on *XMM-Newton* EPIC-pn data as they provide the highest source count rate. The observation data files (ODF) and the Pipeline Processing System (PPS) calibrated event lists of each observation are retrieved from the *XMM-Newton* Science Archive (XSA). These observations are then further processed using the *XMM-Newton* Science Analysis Software (SAS v21.0.0) ¹.

All the event files have been re-screened to remove background flares. To do so we create a single event (PATTERN=0), high energy (10-12 keV) light curve, for each observation. We visually inspect all these light curves and determine the threshold count rate (roughly varying between 0.1 and 0.5 count/s) be-

Table 1. "Known AGN" sample

Applied criteria	number
WISE colors	146
$z < 0.02$	113
X-ray observations	102

low which the light curve is low and steady. Then we create the good time interval (GTI) file for each observation using `TABGTI-GEN` task.

In our analysis only single and double events, (i.e., PATTERN \leq 4 for the EPIC PN) have been used and, in addition, the flag=0 selection expression has been applied to reject events which are close to CCD gaps or bad pixels.

We define a circular region of 15 arcsec radius for the source area and a 50 arcsec nearby source-free region for the background estimation. Then the source and background files are produced using `EVSELECT` task and the corresponding auxiliary files using `RMFGEN` and `ARFGEN` tasks. All the spectra have been grouped to give a minimum of 15 counts per bin.

3.2. *NuSTAR* data reduction

The *NuSTAR* observations are processed using the data analysis software *NuSTARDAS* v2.1.2 and *CALDB* v.20231017 ². We have downloaded the calibrated event list files from the *NuSTAR* archive. Inspection of these cleaned event files shows no further affection by flaring events.

Then we extract source and background event files for each of the two *NuSTAR* focal plane modules (FPMA & FPMB) using the `NUPRODUCTS` script. We adopt a radius of 60 arcsec for the source spectral extraction, for both FPMA & FPMB. The background spectra are extracted from a four times larger (120 arcsec radius) source-free region of the image at an off-axis angle close to the source position.

3.3. *Chandra* data reduction

During the single *Chandra* observation presented here, the ACIS was operated in the ACIS-S mode. Our data reduction for the *Chandra* observation is performed using *CIAO* v.4.15 and the *CALDB* version 4.10.7. We use the level 2, fully calibrated events, provided by the *Chandra* X-Ray Center standard pipeline process. We extract the spectral and the ancillary files using the `SPEXTRACT` script in *CIAO*. The source spectrum, is extracted from a circular area of 5 arcsec radius while the background spectrum was extracted from a nearby, source-free circle of 20 arcsec radius. The spectrum is grouped using the `GRPPHA` task in `FTOOLS` to a minimum number of 15 counts per bin.

4. Spectral analysis

In this work we present the X-ray spectral analysis for twelve sources. Eleven sources are presented here for the first time while IC4995, already presented in Osorio-Clavijo et al. (2022), has been re-analyzed with a model more suitable to its Compton-thick nature. The spectral fitting was carried out using *XSPEC* v12.13.1 (Arnaud 1996). We simultaneously fit all the available spectra for each source.

¹ https://xmm-tools.cosmos.esa.int/external/xmm_user_support/documentation/sas_usg/USG.pdf

² https://heasarc.gsfc.nasa.gov/docs/nustar/analysis/nustar_swguide.pdf

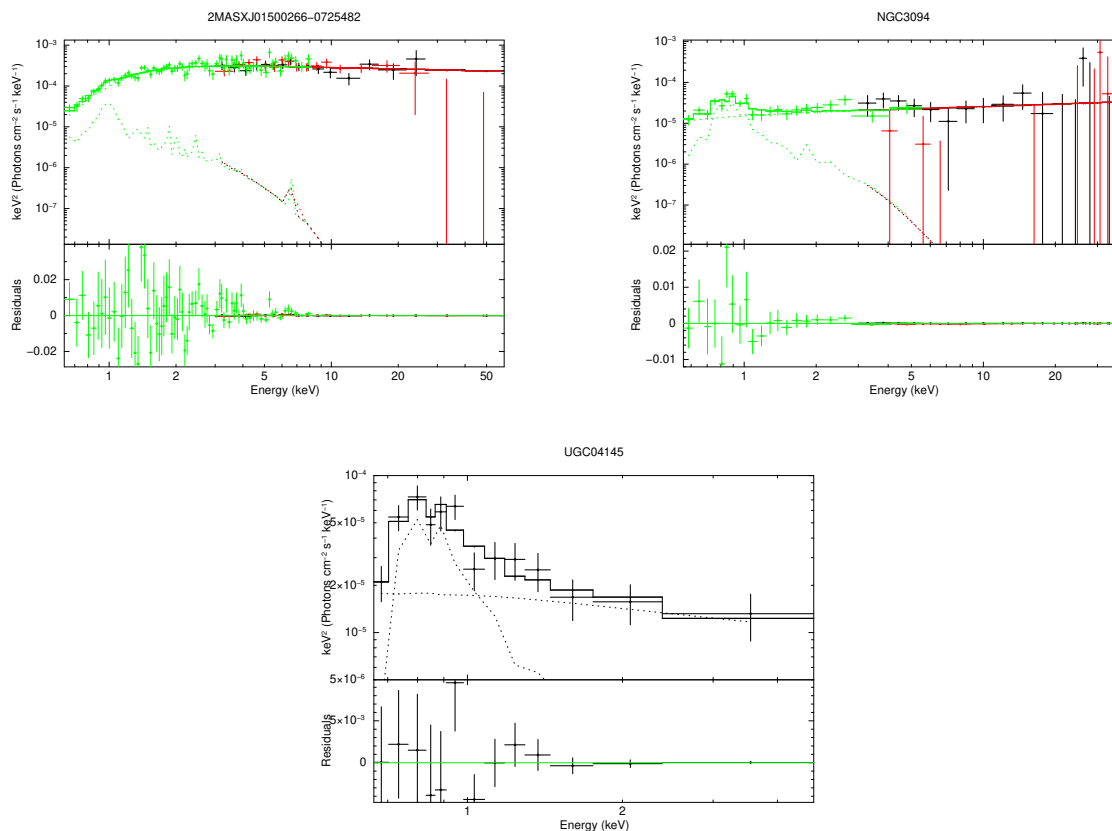


Fig. 2. X-ray spectra, best fit model and residuals for the sources fitted with the simple model.

4.1. Single power-law model

Initially, we utilize a simple model consisting of an absorbed power-law model (PO) to describe the AGN continuum X-ray emission. We also try to add a Gaussian component (GA) to account for the $\text{FeK}\alpha$ emission line and/or a thermal model (APEC) and/or a second soft power-law to accommodate the possible presence of starforming or scattered soft X-ray emission. These additional components are added to the data when they provide an improvement to the fit at the 90 per cent confidence level.

The full XSPEC notation of our model is $\text{PHABS}_{\text{GAL}}*(\text{APEC}+\text{PO}+\text{zPHABS}*\text{PO}+\text{zGA})$. The Galactic value of the equivalent hydrogen column for the photoelectric absorption model (PHABS) is being fixed to the value obtained from Dickey & Lockman (1990) while the intrinsic column density of the source is free to vary. The source redshift is also fixed to the spectroscopic values presented in Table 2. The abundances have been fixed to the default abundance table values in XSPEC and the width of the Gaussian line is also freeze to 0.01 keV.

Only three sources are consistent with this model. The reduced χ^2 which is close to one suggests a good fit. These lack a strong absorption or high $\text{FeK}\alpha$ equivalent width. The spectral fitting results for these three sources are listed in Table 3. In particular, we list the value of the plasma temperature for the thermal model, the photon index of the power-law along with the estimated amount of obscuration, the equivalent width of the $\text{FeK}\alpha$ line and normalization parameters of the continuum. A goodness of fit estimator is also presented using the χ^2 statistic over the degrees of freedom (χ^2/dof). All the errors correspond

to the 90% confidence level. Moreover, Table 6, lists the estimated flux and luminosity values for each component used in the fitting. In particular, we provide the observed flux of the soft components and the continuum flux in the 0.5-2, 2-10 and 10-80 keV bands. Estimates in the ultra hard 10-80 keV band are presented only when *NuSTAR* data are available. We also present the intrinsic luminosity measurements of the same components by zeroing the value of the intrinsic column density in the best fit model.

In Fig. 2 we plot the unfolded spectrum, the best fit model and the residuals in $E^2f(E)$ units. This representation visualises the spectral fitting results and distinguishes between the different spectral components. Note that in an $E^2f(E)$ plot a photon index of $\Gamma = 2$ is represented by a horizontal line. The thermal emission is shown as an increase above the hard X-ray continuum in the lower energies, while absorption effects appear as a constant decline of the spectrum towards lower energy part of the spectrum.

4.2. RXTORUS model

For the majority of the sources, the spectral fitting results using the above simple model do not provide an acceptable fit. This is primarily due to the estimated column density being sufficiently high, close to or exceeding the Compton-thick limit. Consequently, Thompson scattering effects must also be considered through appropriate modeling. Moreover, in these cases, reflected emission may be a dominant process in shaping of the hard X-ray spectrum. If not properly addressed, this can result

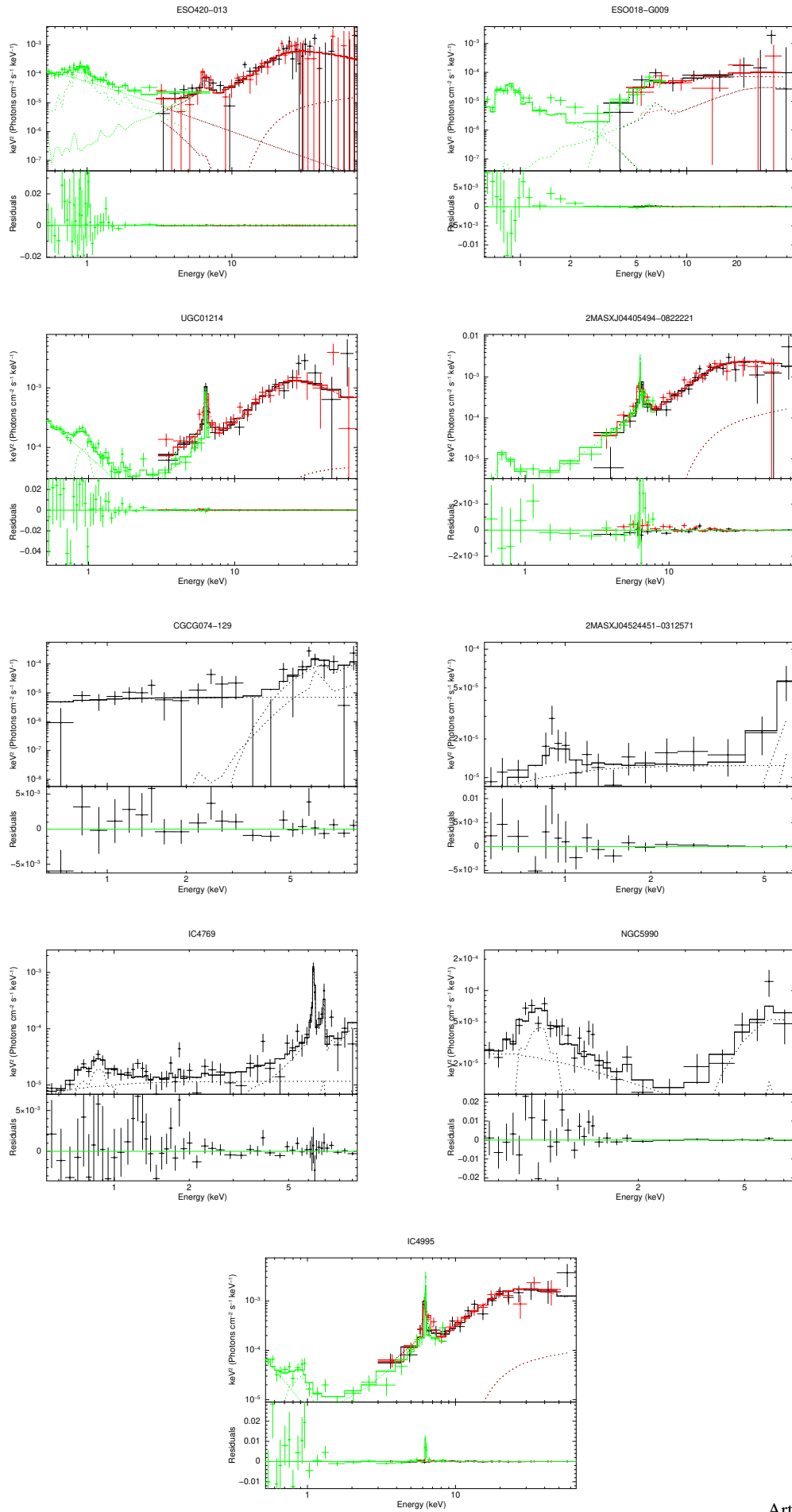


Fig. 3. X-ray spectra, best fit model and residuals for the sources fitted with the 'RXTORUS model.

in unrealistic X-ray spectral indexes and inaccurate fitting outcomes.

To address these complexities we opt to utilize the RXTORUS model introduced by Paltani & Ricci (2017). This model self-consistently addresses (a) the transmitted continuum, containing only photons that did not interact with the surrounding material, (b) the scattered continuum, containing all photons that underwent one or more Compton scatterings, but no photo-ionization or fluorescence and (c) all photons that underwent at least one photo-ionization and subsequent fluorescence re-emission, in addition to any number of Compton scatterings.

The free model parameters are (a) the power-law photon index, (b) the column density along the line-of-sight, (c) the equatorial column density of the torus, (d) the inclination angle, defined as the angle between the normal to the plane of the torus and the observer, (e) the opening angle of the torus defined as the ratio of the inner to the outer radius of the torus and (f) the normalization factor. In our case we use the RXTORUS model grid calculated with a pre-fixed high energy cut-off value of 200 keV, and the abundances are fixed to the default abundance table values used in the XSPEC (Anders & Grevesse 1989). In our set-up we assume a simple torus geometry and therefore the equatorial column density and the line-of-sight obscuration are tied using Eq. 1 in Paltani & Ricci (2017). Also, the normalization parameters of the reprocessed emission are tied to the normalization of the continuum.

As in the case of the simple modeling presented above, we check for the presence of a thermal model (APEC) and/or a second soft power-law to account for any starforming or scattered soft X-ray emission. These additional components are added to the data when they provide an improvement to the fit at a 90 per cent confidence level at least. The XSPEC notation of this model is PHABS_{GAL} * (PO + APEC + RXTORUS), where the RXTORUS notation corresponds to the XSPEC command atable(RXTORUS reprocessed component)+etable(RXTORUS continuum component)*CUTOFFPL.

In specific cases, depending on the quality of the data and model complexity, we choose to freeze certain model parameters to aid in fitting and prevent convergence issues. Thus, the photon index is sometimes fixed at the value of $\Gamma = 2$, the viewing angle is set to 90 degrees (edge-on) and the ratio of the inner to the outer radius is fixed at 0.5, corresponding to a half torus opening angle of 60 degrees.

The spectral fitting results using the above spectral model are presented in Table 4. In detail, we list the thermal model plasma temperature, the photon index of the scattered emission (Γ_{soft}), the photon index of the continuum power-law along, the obscuration along the line of sight, and the corresponding equatorial column density. The values for the torus opening angle and the viewing angle are also listed in the same table. An estimate of the goodness-of-fit is also provided using $\chi^2/\text{d.o.f.}$ ratio. Model components that are not statistically significant are omitted from the table. Fixed parameter values and upper limit estimations are clearly indicated in the table. All errors correspond to the 90% confidence interval. Notably, all the sources are reasonably well fit using the RXTORUS model. Moreover, in Table 7, we provide a comprehensive summary of the estimated flux and luminosity for each of the model components used in the fitting as discussed previously in the case of the simple spectral modeling. Additionally, in Fig. 3 we plot the unfolded spectrum, the best fit model and the residuals in $E^2f(E)$ units.

Our spectral analysis suggests that all sources present column densities exceeding 10^{23}cm^{-2} . In particular, there are four Compton-thick sources, reported for the first time in the lit-

erature: ESO420-013, UGC01214, 2MASXJ04405494-0822221 and IC4769. In three cases we can only provide a lower limit on N_{H} estimation utilizing both *NuSTAR* and *XMM-Newton* data. Only in the case of IC4769 the N_{H} constrain is tighter, achieved however by fitting the only available *XMM-Newton* data with a fixed photon index. A common characteristic is the very prominent FeK α emission line, present in all the individual observations. This further supports the presence of high amounts of obscuring material along their line of sight.

In all sources strong soft excess emission is being observed, originating from optically thin collisionally ionized hot plasma (APEC model component). Additionally, most sources require an additional scattered emission component (soft power-law component) to adequately fit the soft X-ray data. When the data do not provide a reasonable constraint, the photon indices of both the soft and hard power-law components are tied and fixed to a value of $\Gamma = 2$. However, in certain cases, decoupling the photon index of the scattered emission from that of the intrinsic emission as suggested by, in Silver et al. (2022) and Yamada et al. (2021)) leads to a significantly improved spectral fits.

4.3. UXCLUMPY model

For the five Compton-thick sources presented in Table 4 we repeat the spectral fitting analysis using the UXCLUMPY model (Buchner et al. 2019). This model is constructed to reproduce the column density distribution of the AGN population and cloud eclipse events in terms of their angular sizes and frequency. The model assumes a clumpy structure for the obscuring material and applies a second Compton thick reflecting layer close to the corona. Our motivation is to verify the Compton-thick nature of these sources using a substantially different fitting model. An equally important task is to explore whether the UXCLUMPY model, allowing for much higher values for the column density than any other model, up to the 10^{26}cm^{-2} , could provide tighter constraints for the column density of these sources. To this end we use a similar setup as described previously; however all the geometrical parameters have been kept fixed. The viewing angle, measured from the vertical symmetry axis toward the equator has been fixed to 90 degrees. The σ_{torus} parameter (TORsigma in XSPEC table model) that describes the dispersion of the cloud population has been fixed to 30 degrees, and the covering factor of the Compton thick inner reflecting layer, (CTKcover parameter), has been fixed to 0.4. The results are presented in Table 5. The new spectral fitting results verify the Compton-thick nature of these sources. However, we are still unable to further constrain the N_{H} values which still appear as lower limits.

5. Discussion

We organise our discussion as follows. In Section 5.1 we present the N_{H} distribution among the "known AGN" sample. In section 5.2 we discuss about the prospects of finding a large number of Compton-thick AGN among the "new AGN" sample which has no BAT detections. It is likely that a number of Compton-thick sources may lie among the AGN that are not selected by the *WISE* criteria. This is discussed in section 5.3. In section 5.4 we discuss the Compton-thick AGN that may be lurking among the fainter AGN sub-sample with luminosities $\log L(12\mu\text{m})[\text{erg s}^{-1}] < 42.3$. In section 5.5 we discuss the possible dependence of the fraction of either obscured or Compton-thick AGN on luminosity. Finally, in section 5.6 we argue on the existence of extremely obscured AGN with $N_{\text{H}} > 10^{25}\text{cm}^{-2}$.

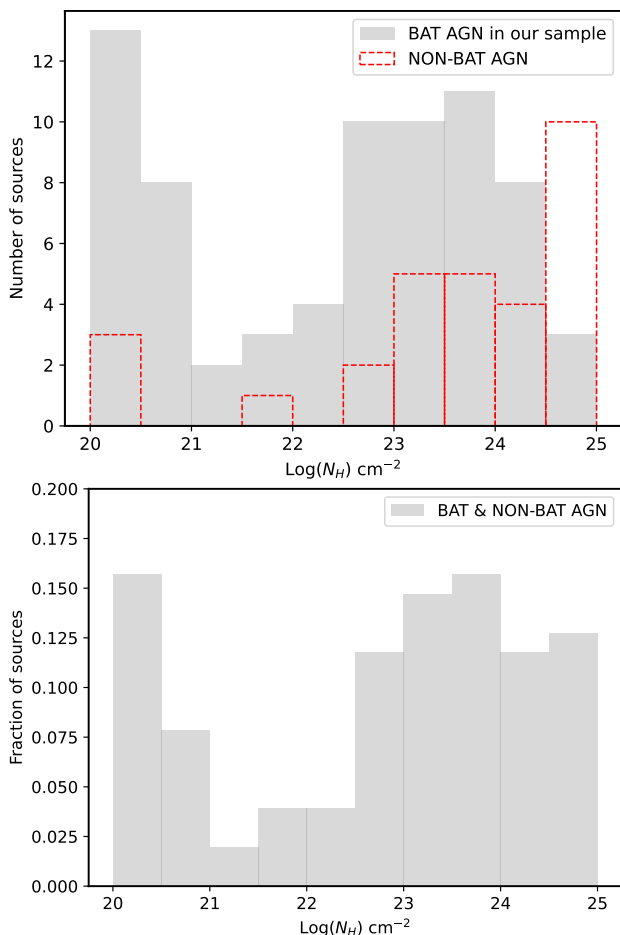


Fig. 4. (a) Upper panel: Comparison of the N_H distribution for the sources in our sample detected in *Gehrels/Swift* /BAT 70 months all sky survey (grey-shaded histogram) with those missed (red-dashed line). (b) Lower panel: The N_H distribution for the total population

5.1. The Compton-thick sources in the 'known AGN' sample

While X-ray surveys offer the most unobscured view towards the nucleus, when these sources are obscured by material close to or above the Compton thick limit - where the Compton scattering processes dominate over photo-ionization - the X-ray sources suffer from significant attenuation hindering their detection. This results to a bias in the sense that higher column density sources, are under-represented in flux-limited surveys, even those in the BAT ultra hard X-ray band. Hence, the recovery of the true fraction of Compton-thick AGN, even in the local universe, remains problematic. Our analysis enables us to study the distribution of obscuration in the local universe in a nearly unbiased way as it is based on a complete volume limited galaxy sample.

In Fig. 4 we present the N_H distribution, along the line of site, for the sources in our sample. The upper panel compares the N_H distribution of the 70-month BAT AGN existing in our sample (grey-shaded histogram) with the N_H distribution of the sources missed by the hard X-ray survey (red-dashed line). The bottom panel shows the total N_H distribution of our sources. Notably, the vast majority of the sources missed by the BAT survey (14 out of 30) are associated with Compton-thick sources corresponding to a fraction of 45%. This clearly suggests that below the BAT flux limit, lurks a population of Compton-thick AGN which evade detection. For all the 102 sources in our sample the fraction of Compton-thick AGN is 25/102 or $25 \pm 5\%$.

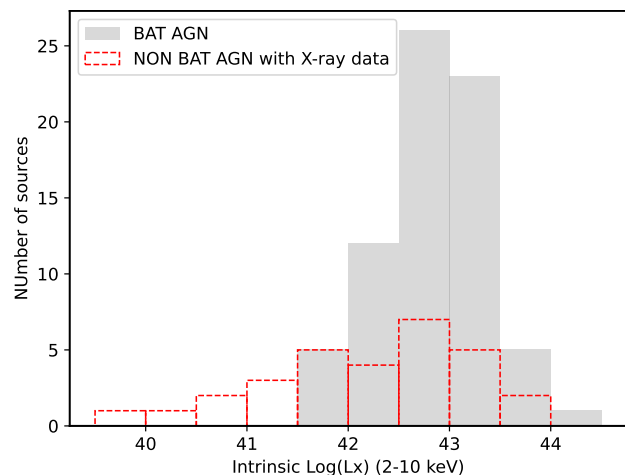


Fig. 5. Comparison of the 2-10 keV luminosity distribution for the sources detected in *Gehrels/Swift* /BAT 70 months all sky survey (grey-shaded histogram) with those missed (red-dashed line).

In Fig. 5 we compare the intrinsic 2-10 keV luminosity distribution of the BAT detected and non-detected sample. It is noteworthy that a non-negligible number of sources within the non-BAT sample, extends to lower luminosities, $L_x < 10^{41.5} \text{ erg s}^{-1}$ forming a tail in the distribution. The vast majority of these sources are not Compton-thick. Two of these have been analysed for the first time here, namely NGC3094 an UGC04145 showing no evidence for significant obscuration. Another source, (NGC2623) is moderately obscured (Yamada et al. 2021) while only NGC660 shows evidence for significant obscuration Annuar et al. (2020). This suggests that a number of sources remain undetected by BAT because they have a low intrinsic luminosity rather than being associated with Compton-thick sources. Similar conclusions are drawn by Yamada et al. (2021, 2023) in a sample of nearby ultra-luminous infrared galaxies.

An unknown factor that may affect our estimations is the number of sources lacking X-ray information. For these sources the column density and the X-ray luminosity remain unknown, and as a result, they have not been included in the analysis. In Fig. 6 we compare the redshift and the 12 micron luminosity, $L_{12\mu\text{m}}$, derived from Asmus et al. (2020), with the rest of our sample. The redshift distribution of the X-ray undetected sources shows no difference compared to the rest of the sample. However, the $L_{12\mu\text{m}}$ distribution clearly occupies the low luminosity part of the distribution $L_{12\mu\text{m}} < 10^{43} \text{ erg s}^{-1}$. This suggests that a number of sources have not been detected because they have low luminosities rather than they are associated with Compton-thick nuclei. In the extreme case, where we assume that all eleven sources without X-ray information are associated with Compton-thick AGN, the fraction would rise to $32 \pm 5\%$.

5.2. WISE selected AGN with no X-ray data available

So far we have discussed the properties of the "known AGN" sample, containing as explained at section 2, *WISE* selected AGN, already known to host an active nucleus in the literature. As we mentioned Asmus et al. (2020) define an additional AGN sample or the "new AGN" sample, containing *WISE* selected AGN, using the same criteria, but without any prior AGN classification in the literature. This sample comprises of 32 "new" AGN. At first glance one would expect that the fraction of Compton-thick AGN is high and hence the "new" AGN re-

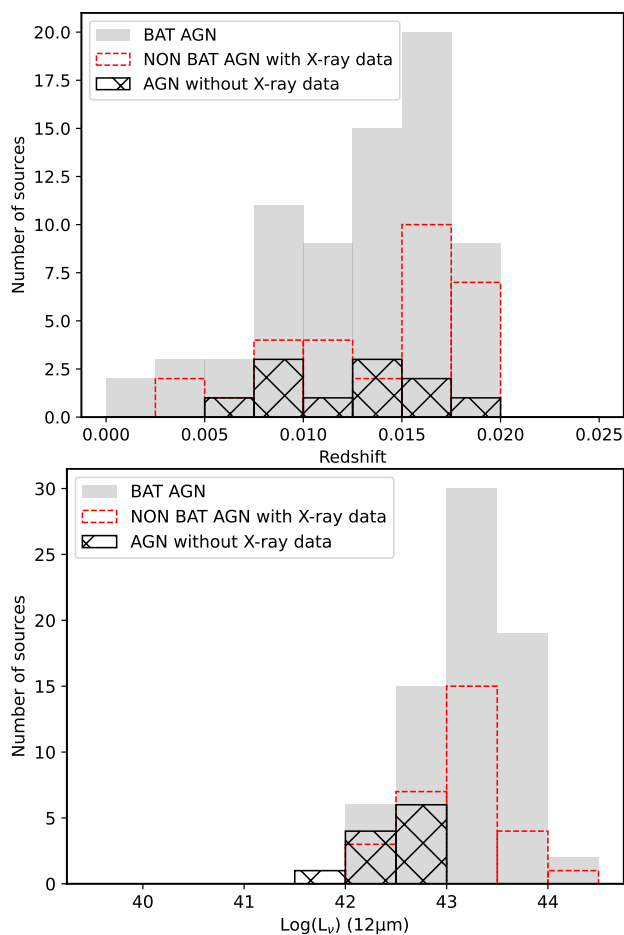


Fig. 6. (a) Upper panel: Comparison of the redshift distribution for the sources in our sample according to their origin. Sources found in BAT surveys are shown with gray histogram, sources with X-ray data missed by BAT survey are displayed with red-dashed line and sources without X-ray data are shown with the hatched histogram. (b) Lower panel: Similar as above for the $L_{12\mu\text{m}}$ luminosity obtained from Asmus et al. (2020).

main undetected by BAT. Indeed, the fraction of Compton-thick AGN in the "known AGN" sample that were undetected by BAT was particularly high of the order of 45%. The comparison of the $L_{12\mu\text{m}}-z$ distribution of the BAT AGN and the "new AGN" sample (Fig. 7) sheds more light on the reasons why the latter sample may remain undetected in BAT. The distribution of the "new AGN" sample is clearly skewed towards lower luminosities and higher redshift. This suggests that a number of the "new" AGN may remain undetected by BAT because of their low luminosity, provided that there is a strong correlation between the $L_{12\mu\text{m}}$ and the X-ray luminosity as found in Asmus et al. (2015) and Stern (2015). According to the above diagram, the most strong candidates for being Compton-thick sources are a handful of sources that mingle with the "known AGN" sample in the same luminosity-redshift area.

5.3. Compton-thick AGN missed by the WISE criteria

A number of well-known, BAT detected, Compton-thick AGN are not present in our sample. This is because of the applied AGN selection criteria, based on *WISE* colours presented in section 2. For example a number of low luminosity AGN or those where

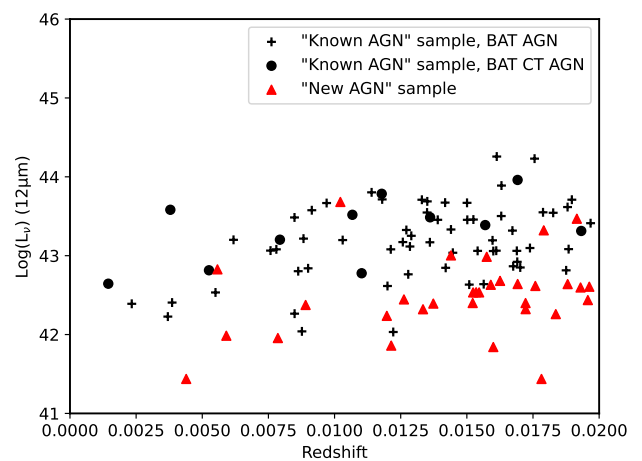


Fig. 7. The $L_{12\mu\text{m}}$ vs redshift distribution of the BAT AGN against the "new" AGN sample.

the emission from the host galaxy dominates over the AGN may be missed by the W1-W2 criterion (e.g. Pouliaxis et al. 2020). Then, a question that arises is whether our sample selection criteria affect the *fraction* of detected Compton-thick sources.

In order to investigate this issue we examine the sample of Compton-thick AGN compiled by the Clemson group (e.g. Marchesi et al. 2018; Zhao et al. 2021; Torres-Albà et al. 2021). These Compton-thick AGN were originally selected from the BAT AGN catalogue. Then the column density was accurately determined by means of *NuSTAR* observations. There are 17 bona fide Compton-thick AGN in the Clemson sample³ within $z < 0.02$. Only eight out of these 17 Compton-thick sources follow our selection criteria presented in section 2, while nine Compton-thick sources in the Clemson sample do not and therefore have been missed from this study. However, in a similar manner, in *Gehrels/Swift* /BAT 70 months all sky survey there are approximately 145 sources identified as AGN within $z < 0.02$ according to Baumgartner et al. (2013). From this sample, half of the sources (72) satisfy the same *WISE* selection criteria while the other half (73) have been missed. This exercise clearly demonstrates that our selection criteria equally affect all the BAT population and not preferentially the highly obscured sources and therefore the measured fraction of Compton thick sources remains unaffected, at least for the fluxes probed by the *Gehrels/Swift* /BAT 70 months all sky survey.

5.4. Compton-thick AGN at faint luminosities

Up to this point, we have discussed the presence of Compton-thick sources among luminous AGN with luminosities $\log L(12\mu\text{m})[\text{erg s}^{-1}] > 42.3$ regardless of their blue or red W1-W2 colours. However, Asmus et al. (2020) point out that 70% of known Seyferts have luminosities below this threshold. This means that an appreciable number of low-luminosity Compton-thick AGN may remain undetected. We use the relation of hard X-ray luminosities vs. the nuclear MIR luminosities (e.g. Gandhi et al. 2009; Asmus et al. 2011) to convert our $12\mu\text{m}$ luminosity threshold to a 2-10 keV X-ray luminosity threshold. We find that the corresponding 2-10 keV X-ray luminosity is approximately $\log L_X[\text{erg s}^{-1}] > 42.2$. It has been suggested that the fraction of obscured AGN increases with decreasing luminosity or decreasing Eddington ratio (e.g. Akylas et al. 2006;

³ <https://science.clemson.edu/ctagn/>

Ezhikode et al. 2017; Ueda et al. 2014). However, at very low luminosities this trend may be reversed. According to theoretical models no torus is formed at very low bolometric luminosities, $L_{\text{BOL}} < 10^{42}$ erg s $^{-1}$ (Elitzur & Shlosman 2006). In any case, such a population of low luminosity Compton-thick AGN may indeed exist without violating the hard X-ray and mid-IR background constraints (Comastri et al. 2015; Nardini & Risaliti 2011). We note here that, Boorman et al. (2024) presented simulations, suggesting that the new High-Energy X-ray Probe-class mission concept (HEX-P) will be able to measure intrinsic luminosities and line-of-sight column densities but also distinguish between obscuration geometries of this low luminosity population.

5.5. Dependence of obscuration on luminosity

Next, we investigate whether there is a dependence of the Compton-thick fraction on intrinsic luminosity. If for example the fraction of Compton-thick AGN increases with decreasing luminosity, this could imply that the X-ray undetected sources in our sample harbour more heavily obscured sources. Previous results on this subject remain controversial. In particular Brightman et al. (2015) found possible evidence of a strong decrease of the covering factor of the torus while Buchner et al. (2015) found instead that the fraction of Compton-thick AGN is compatible with being constant with the X-ray luminosity. Also, Ricci et al. (2015) analyzed the data from the *Gehrels/Swift* /BAT all-sky survey and provided the corrected for selection bias, intrinsic column density distribution of Compton-thick AGN in the local universe in two different luminosity ranges. Their average estimated fraction of Compton-thick sources is $27 \pm 4\%$. They also present tentative evidence for a small decrease in the fraction of obscured Compton-thick AGN with increasing luminosity. In Fig. 8 we present the fraction of the Compton-thick sources in our sample as a function of the 2-10 keV and the 12 micron luminosity. The errors in the estimated Compton-thick fraction correspond to the 1σ confidence level and the uncertainty in the luminosity denotes the range of each luminosity bin. Clearly, the plots show no evidence for any dependence of the Compton-thick fraction with luminosity. Our results indicate a very similar fraction of Compton-thick sources at all luminosity bins, fully consistent with the average value of $25 \pm 5\%$. However the limited statistics do not allow to rule out changes at the level of the quoted errors.

Next, we plot the fraction of the obscured sources ($N_{\text{H}} > 10^{22}$ cm $^{-2}$) as a function of the intrinsic luminosity in Fig. 9. Previous studies (e.g. Ueda et al. 2003; Akylas et al. 2006; Buchner et al. 2015; Ricci et al. 2015) suggest a clear decline in the fraction of obscuration with decreasing X-ray luminosity. Our analysis does not reveal any such trend in contradiction to the studies above. However, this trend has been previously identified across a much broader luminosity range than the one explored here. It is the highest luminosity bins that are not covered here, that play a significant role in this trend (e.g. Ueda et al. 2003).

Alternatively, Sazonov et al. (2015), claim that this effect could be purely artificial due to a negative bias in finding obscured sources and a positive bias in finding unobscured AGN, due to the reflected emission. According to these authors, the above biases lead to a decreasing observed fraction of obscured AGN with increasing luminosity even if there is no intrinsic luminosity dependence. In this scenario, the current analysis correctly finds a constant fraction of obscured sources in all luminosities.

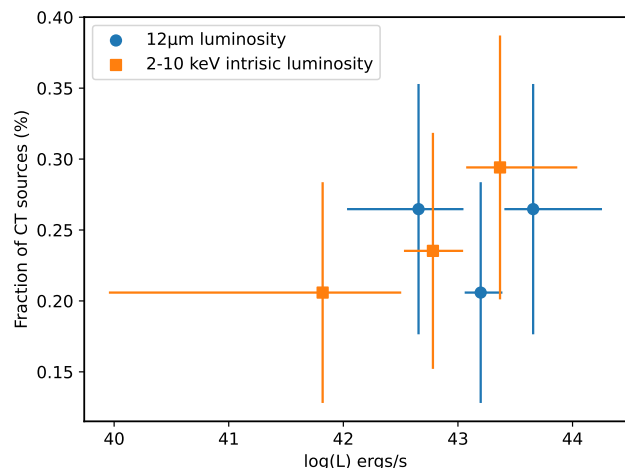


Fig. 8. Fraction of the Compton-thick sources ($N_{\text{H}} > 10^{24}$ cm $^{-2}$) in our sample as a function of the intrinsic 2-10 keV luminosity (blue-squared points) and the 12 micron luminosity (orange-circled points). The error in the estimated fraction corresponds to the 68 per cent confidence level while the uncertainty in the luminosity axis denotes the range of each luminosity bin used.

5.6. Extreme obscuration in the local universe

Our work so far has provide a robust and almost unbiased constraint of the Compton-thick fraction among the bright, WISE selected AGN in the local Universe. One key element, which has not been addressed, is the distribution of the column density among the Compton-thick sources. Most X-ray background synthesis models assume either a flat fraction of Compton-thick AGN over the entire range of $\log(N_{\text{H}})[\text{cm}^{-2}] = 24 - 26$ (e.g. Ananna et al. 2019; Ueda et al. 2014; Gilli et al. 2007) or alternatively, all Compton-thick AGN are placed in the range of $\log(N_{\text{H}})[\text{cm}^{-2}] = 24 - 25$ (e.g. Akylas et al. 2016). Our observational leverage on the distribution remains uncertain. The only two known Compton-thick AGN which may have column densities close to $\sim N_{\text{H}} = 10^{25}$ cm $^{-2}$ are Circinus and NGC1068. The dearth of such highly obscured sources in the BAT surveys is possibly because the extreme obscuration prohibits their detection even at distances as low as 100 Mpc (e.g. Burlon et al. 2011). The limited N_{H} range of the current Compton-thick spectral models, which typically have a ceiling in the maximum allowed N_{H} value of 10^{25} cm $^{-2}$, further complicates the secure identification of the most heavily obscured of the Compton-thick sources.

Our sample which does not suffer from any flux-limit bias offers the opportunity to further address this issue. We arbitrarily assume that all the Compton-thick sources with lower limit column density estimations $N_{\text{H}} > 10^{24}$ cm $^{-2}$, occupy the $\log(N_{\text{H}})[\text{cm}^{-2}] = 25 - 26$ bin. All the other Compton-thick sources - those with a secure measurement in their N_{H} - are then placed in the $\log(N_{\text{H}})[\text{cm}^{-2}] = 24 - 25$ bin. According to Table A.1, there are 25 Compton-thick sources in our sample and only in eight cases the N_{H} estimation is a lower limit. Then, this crude approximation shows that the fraction of $\log(N_{\text{H}})[\text{cm}^{-2}] = 25 - 26$ sources account roughly for at most 30% of the Compton-thick population at least in the 'known AGN' sample.

6. Summary

We analysed the X-ray properties of the Asmus et al. (2020) paper of local ($z < 0.02$) AGN. Our basic goal is to constrain

Table 2. Log of sources analysed in this work

Source name	<i>Chandra</i>		<i>XMM-Newton</i>		<i>NuSTAR</i>	
	OBSID	Exp. (s)	OBSID	Exp. (s)	OBSID	Exp. (s)
2MASXJ01500266-0725482	-	-	0200431101	11921	60360005002	30725
2MASXJ04405494-0822221	-	-	0890690401	18000	60701043002	30706
2MASXJ04524451-0312571	-	-	0307002501	18111	-	-
CGCG074-129	-	-	0822391201	13600	-	-
ESO018-G009	-	-	0805150401	19200	60362029002	28755
ESO420-013 ¹	10393	12760	-	-	60668003002	108164
IC4769	-	-	0405380501	35013	-	-
IC4995 ²	-	-	0200430601	11912	60360003002	33998
NGC3094	-	-	0655380801	16918	60668001002	100823
NGC5990	-	-	0655380901	18918	-	-
UGC01214	-	-	0200430701	11913	60360004002	31998
UGC04145	-	-	0763460201	18000	-	-

¹ For this source *XMM-Newton* observations were not available. Instead we make use of *Chandra* data.

² X-ray spectral analysis has been presented in Osorio-Clavijo et al. (2022). Here we have repeated the analysis using spectral modeling suitable to the Compton thick nature of the source.

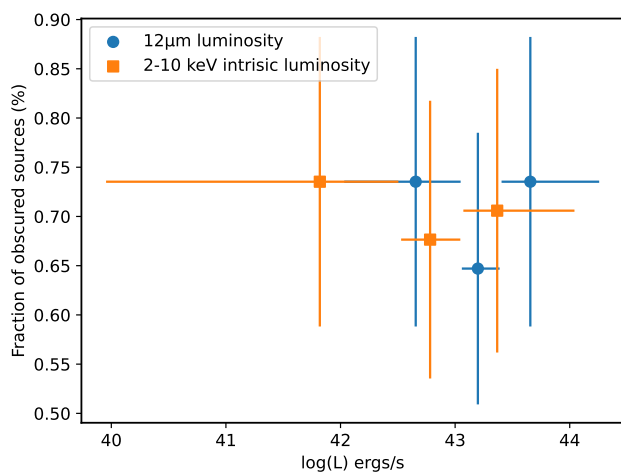


Fig. 9. Fraction of the obscured sources ($N_{\text{H}} > 10^{22} \text{ cm}^{-2}$) as a function of the intrinsic 2-10 keV luminosity (blue-square points) and the 12 micron luminosity (orange-circle points). The error in the estimated fraction corresponds to the 68 per cent confidence level while the uncertainty in the luminosity axis denotes the range of each luminosity bin used.

the number density of Compton-thick sources. We primarily focus on the AGN sample selected on the basis of the *WISE* W1 and W2 colours. This is divided in two subsamples. The “known AGN” sample, already known to host an active nucleus in the literature, that contains 113 sources of which the vast majority (102) have been observed by various X-ray missions (72 have been detected by BAT) and the “new AGN” sample which contains 32 sources which have no prior AGN classification in the literature. For the first sample, we compile the X-ray observations available in the literature. We also analyse here for the first time, the *NuSTAR*, *XMM-Newton* and *Chandra* observations of eleven sources. As the sample examined here is not flux-limited, it provides us with the best opportunity so far to study the full Compton-thick AGN population. Our results can be summarised as follows.

- Our spectral analysis employing both the RXTORUS and the UXCLUMPY models reveals four new Compton-

thick sources with column densities in excess of $4 \times 10^{24} \text{ cm}^{-2}$

- The fraction of Compton-thick sources among the 102 sources with available X-ray data in the “known AGN” sample is $25 \pm 5\%$. Even in the extreme case where all the sources with no available X-ray data were associated with Compton-thick AGN the Compton-thick fraction would rise to $31 \pm 5\%$
- The fraction of Compton-thick AGN among the 30 sources that have not been detected by BAT is much higher (44%) compared to the fraction of the Compton-thick sources in the BAT detected sources which is only 16%.
- Regarding the “new AGN” sample, we argue that most of these sources have not been detected by BAT because they have low luminosity rather than high obscuration.

Table 3. Spectral fitting results using the simple power-law model

Source name	Mission ¹	PHABS _{GAL} * (APEC + PHABS * PO + GA) model parameters									
		kT	N _{APEC}	Γ _{soft} PO	Γ _{hard} PO	N _H	N _{hard} PO	FeK line (EW)	χ ² /dof		
		keV	×10 ⁻⁵	×10 ⁻⁵	×10 ⁻⁵	×10 ²² cm ⁻²	×10 ⁻³	eV			
2MASXJ01500266-0725482	X,N	-	-	-	-	2.11 ^{+0.10} _{-0.10}	0.36 ^{+0.08} _{-0.06}	6.43 ^{+0.25} _{-0.10} (290 ⁺¹⁹⁰ ₋₁₅₀)	115.99/103		
NGC3094	X,N	0.77 ^{+0.10} _{-0.12}	0.87 ^{+0.74} _{-0.33}	-	-	1.92 ^{+0.41} _{-0.28}	0.021 ^{+0.018} _{-0.014}	-	48.89/40		
UGC04145	X	0.68 ^{+0.11} _{-0.13}	1.24 ^{+0.69} _{-0.64}	-	-	2.43 ^{+1.35} _{-0.83}	0.019 ^{+0.073} _{-0.010}	-	6.7/8		

¹ X: *XMM-Newton* data have been used, C: *Chandra* data have been used, N: *NuSTAR* data have been used

Table 4. Spectral fitting results using the RXTORUS model

Source name	Mission ¹	PHABS _{GAL} * (PO + APEC + RXTORUS) model parameters										
		Γ _{soft}	N _{soft}	kT	N _{APEC}	Γ	N _H ^{eq}	N _H ^{los}	θ _{inc}	sin(φ _{torus})	N _{RXTORUS}	χ ² /dof
			×10 ⁻⁵	keV	×10 ⁻⁵		×10 ²² cm ⁻²	×10 ²² cm ⁻²	deg.		×10 ⁻³	
ESO420-013	C,N	3.77 ^{+0.37} _{-0.29}	5.83 ^{+2.79} _{-2.51}	0.89 ^{+0.08} _{-0.09}	3.14 ^{+2.20} _{-1.23}	2(f)	>508	>300	77 ⁻⁶ ₋₂	0.5(f)	9.84 ^{+6.75} _{-7.39}	101.2/96
ESO018-G009	X,N	-	-	0.75 ^{+0.10} _{-0.10}	0.91 ^{+0.19} _{-0.12}	2(f)	31 ⁺²⁴ ₋₁₇	31 ⁺²⁴ ₋₁₇	90(f)	0.5(f)	10.77 ^{+2.30} _{-4.41}	40.51/31
UGC01214	X,N	4.52 ^{+0.42} _{-0.33}	14.34 ^{+4.91} _{-3.86}	0.92 ^{+0.09} _{-0.08}	4.78 ^{+1.92} _{-1.63}	2(f)	>598	>505	69 ⁺⁴ ₋₃	0.5(f)	7.01 ^{+2.62} _{-1.1}	89.59/73
2MASXJ04405494-0822221	X,N	-	-	0.33 ^{+0.25} _{-0.07}	0.54 ^{+0.25} _{-0.23}	2(f)	>421	>300	69 ⁺⁶ ₋₁₀	0.5(f)	4.16 ^{+8.42} _{-1.33}	74.82/58
CGCG074-129	X	2(f)	0.67 ^{+0.23} _{-0.24}	-	-	2(f)	68 ⁺⁸⁴ ₋₃₇	68 ⁺⁸⁴ ₋₃₇	90(f)	0.5(f)	0.58 ^{+0.43} _{-0.43}	23.01/21
2MASXJ04524451-0312571	X	2(f)	1.24 ^{+0.26} _{-0.26}	1.01 ^{+0.34} _{-0.28}	0.22 ^{+0.23} _{-0.19}	2(f)	>40	>40	90(f)	0.5(f)	0.27 ^{+0.25} _{-0.25}	12.23/14
IC4769	X	2(f)	1.16 ^{+0.24} _{-0.24}	0.76 ^{+0.10} _{-0.10}	0.47 ^{+0.14} _{-0.14}	2(f)	362 ⁺⁵⁷⁷ ₋₁₁₆	362 ⁺⁵⁷⁷ ₋₁₁₆	90(f)	0.5(f)	35.32 ^{+210.57} _{-22.96}	45.89/49
IC4995	X,N	6.01 ^{+2.41} _{-1.32}	0.94 ^{+1.15} _{-0.71}	0.82 ^{+0.13} _{-0.13}	1.04 ^{+0.59} _{-0.55}	2.07 ^{+0.16} _{-0.11}	>815	>482	64 ⁺¹³ ₋₆	0.5(f)	9.53 ^{+14.19} _{-2.80}	66.62/54
NGC5990	X	2.91	2.40 ^{+0.42} _{-0.42}	0.75 ^{+0.11} _{-0.11}	1.21 ^{+0.29} _{-0.29}	2(f)	27 ⁺²⁶ ₋₁₂	27 ⁺²⁶ ₋₁₂	90(f)	0.5(f)	0.12 ^{+0.14} _{-0.05}	30.36/30

¹ X: *XMM-Newton* data have been used, C: *Chandra* data have been used, N: *NuSTAR* data have been used

Table 5. Spectral fitting results of Compton-thick sources only using the UXCLUMPY model

Source name	Mission ¹	PHABS _{GAL} * (PO + APEC + UXCLUMPY) model parameters										
		Γ _{soft}	N _{soft}	kT	N _{APEC}	Γ	N _H ^{eq}	N _H ^{los}	θ _{inc}	(σ _{torus})	N _{UXCLUMPY}	χ ² /dof
			×10 ⁻⁵	keV	×10 ⁻⁵		×10 ²² cm ⁻²	×10 ²² cm ⁻²	deg.		×10 ⁻³	
ESO420-013	C,N	3.35 ^{+0.40} _{-0.24}	5.14 ^{+2.06} _{-2.43}	0.86 ^{+0.08} _{-0.07}	2.55 ^{+0.44} _{-1.21}	1.53 ^{+0.27} _{-0.28}	-	>292	90(f)	30(f)	0.89 ^{+1.42} _{-0.11}	100.83/95
UGC01214	X,N	3.61 ^{+0.26} _{-0.16}	9.61 ^{+0.91} _{-1.01}	0.88 ^{+0.10} _{-0.09}	1.58 ^{+0.60} _{-0.58}	2.33 ^{+0.31} _{-0.22}	-	>345	90(f)	30(f)	16.46 ^{+21.70} _{-7.91}	85.17/72
2MASXJ04405494-0822221	X,N	-	-	0.38 ^{+0.33} _{-0.12}	0.22 ^{+0.18} _{-0.14}	2.17 ^{+0.26} _{-0.21}	-	>298	90(f)	30(f)	18.57 ^{+11.21} _{-6.90}	80.91/58
IC4769	X	-	-	0.75 ^{+0.16} _{-0.16}	0.38 ^{+0.11} _{-0.11}	2.01 ^{+0.34} _{-0.32}	-	>142	90(f)	30(f)	5.12 ^{+6.47} _{-2.97}	71.42/55
IC4995	X,N	5.53 ^{+3.15} _{-1.62}	0.81 ^{+1.41} _{-0.69}	0.79 ^{+0.16} _{-0.14}	0.73 ^{+0.44} _{-0.42}	2.38 ^{+0.11} _{-0.11}	-	>363	90(f)	30(f)	36.6 ^{+28.17} _{-11.53}	86.72/53

¹ X: *XMM-Newton* data have been used, C: *Chandra* data have been used, N: *NuSTAR* data have been used

Acknowledgements. This research is based on observations obtained with *XMM-Newton*, an ESA science mission with instruments and contributions directly funded by ESA Member States and NASA. This research has made use of data from the *NuSTAR* mission, a project led by the California Institute of Technology, managed by the Jet Propulsion Laboratory, and funded by the National Aeronautics and Space Administration. Data analysis was performed using the *NuSTAR* Data Analysis Software (NuSTARDAS), jointly developed by the ASI Science Data Center (SSDC, Italy) and the California Institute of Technology (USA). This research has made use of data obtained from the Chandra Data Archive and the Chandra Source Catalog, and software provided by the Chandra X-ray Center (CXC) in the application packages CIAO and Sherpa. This research has made use of data and software provided by the High Energy Astrophysics Science Archive Research Center (HEASARC), which is a service of the Astrophysics Science Division at NASA/GSFC. This research uses data supplied by the UK Swift Science Data Centre at the University of Leicester.

References

- Ajello, M., Greiner, J., Sato, G., et al. 2008, *ApJ*, 689, 666
- Akylas, A., Georgakakis, A., Georgantopoulos, I., Brightman, M., & Nandra, K. 2012, *A&A*, 546, A98
- Akylas, A. & Georgantopoulos, I. 2009, *A&A*, 500, 999
- Akylas, A. & Georgantopoulos, I. 2021, *A&A*, 655, A60
- Akylas, A., Georgantopoulos, I., Georgakakis, A., Kitsionas, S., & Hatziminaoglou, E. 2006, *A&A*, 459, 693
- Akylas, A., Georgantopoulos, I., Ranalli, P., et al. 2016, *A&A*, 594, A73
- Ananna, T. T., Treister, E., Urry, C. M., et al. 2019, *ApJ*, 871, 240
- Ananna, T. T., Weigel, A. K., Trakhtenbrot, B., et al. 2022, *ApJS*, 261, 9
- Anders, E. & Grevesse, N. 1989, *Geochim. Cosmochim. Acta*, 53, 197
- Annun, A., Alexander, D. M., Gandhi, P., et al. 2020, *MNRAS*, 497, 229
- Arévalo, P., Bauer, F. E., Puccetti, S., et al. 2014, *ApJ*, 791, 81
- Arnaud, K. A. 1996, in *Astronomical Society of the Pacific Conference Series*, Vol. 101, *Astronomical Data Analysis Software and Systems V*, ed. G. H. Jacoby & J. Barnes, 17
- Asmus, D., Gandhi, P., Hönig, S. F., Smette, A., & Duschl, W. J. 2015, *MNRAS*, 454, 766
- Asmus, D., Gandhi, P., Smette, A., Hönig, S. F., & Duschl, W. J. 2011, *A&A*, 536, A36
- Asmus, D., Greenwell, C. L., Gandhi, P., et al. 2020, *MNRAS*, 494, 1784
- Assef, R. J., Prieto, J. L., Stern, D., et al. 2018, *ApJ*, 866, 26
- Baloković, M., Comastri, A., Harrison, F. A., et al. 2014, *ApJ*, 794, 111
- Bauer, F. E., Arévalo, P., Walton, D. J., et al. 2015, *ApJ*, 812, 116
- Baumgartner, W. H., Tueller, J., Markwardt, C. B., et al. 2013, *ApJS*, 207, 19
- Boorman, P. G., Gandhi, P., Alexander, D. M., et al. 2016, *ApJ*, 833, 245
- Boorman, P. G., Torres-Albà, N., Annun, A., et al. 2024, *Frontiers in Astronomy and Space Sciences*, 11, 1335459
- Brightman, M., Baloković, M., Stern, D., et al. 2015, *ApJ*, 805, 41
- Buchner, J., Brightman, M., Nandra, K., Nikutta, R., & Bauer, F. E. 2019, *A&A*, 629, A16
- Buchner, J., Georgakakis, A., Nandra, K., et al. 2015, *ApJ*, 802, 89
- Burlon, D., Ajello, M., Greiner, J., et al. 2011, *ApJ*, 728, 58
- Churazov, E., Sunyaev, R., Revnitsev, M., et al. 2007, *A&A*, 467, 529
- Comastri, A., Gilli, R., Marconi, A., Risaliti, G., & Salvati, M. 2015, *A&A*, 574, L10
- Comastri, A., Setti, G., Zamorani, G., & Hasinger, G. 1995, *A&A*, 296, 1
- Dickey, J. M. & Lockman, F. J. 1990, *ARA&A*, 28, 215
- Elitzur, M. & Shlosman, I. 2006, *ApJ*, 648, L101
- Evans, P. A., Beardmore, A. P., Page, K. L., et al. 2009, *MNRAS*, 397, 1177
- Evans, P. A., Page, K. L., Osborne, J. P., et al. 2020, *ApJS*, 247, 54
- Ezhikode, S. H., Gandhi, P., Done, C., et al. 2017, *MNRAS*, 472, 3492
- Frontera, F., Orlandini, M., Landi, R., et al. 2007, *ApJ*, 666, 86
- Gandhi, P., Fabian, A. C., Suebsuwong, T., et al. 2007, *MNRAS*, 382, 1005
- Gandhi, P., Horst, H., Smette, A., et al. 2009, *A&A*, 502, 457
- Gehrels, N., Chincarini, G., Giommi, P., et al. 2004, *ApJ*, 611, 1005
- Georgantopoulos, I. & Akylas, A. 2019, *A&A*, 621, A28
- Giacconi, R., Gursky, H., Paolini, F. R., & Rossi, B. B. 1962, *Phys. Rev. Lett.*, 9, 439
- Gilli, R., Comastri, A., & Hasinger, G. 2007, *A&A*, 463, 79
- Guo, X., Gu, Q., Xu, J., et al. 2023, *PASP*, 135, 014102
- Haardt, F. & Maraschi, L. 1991, *ApJ*, 380, L51
- Ho, L. C., Filippenko, A. V., & Sargent, W. L. W. 1997, *ApJS*, 112, 315
- Jiang, J., Baloković, M., Brightman, M., et al. 2021, *MNRAS*, 505, 702
- Kammoun, E. S., Miller, J. M., Zoghbi, A., et al. 2019, *ApJ*, 877, 102
- LaMassa, S. M., Yaqoob, T., Boorman, P. G., et al. 2019, *ApJ*, 887, 173
- Luo, B., Brandt, W. N., Xue, Y. Q., et al. 2017, *ApJS*, 228, 2
- Marchesi, S., Ajello, M., Marcotulli, L., et al. 2018, *ApJ*, 854, 49
- Marchesi, S., Ajello, M., Zhao, X., et al. 2019, *ApJ*, 872, 8
- Masini, A., Comastri, A., Baloković, M., et al. 2016, *A&A*, 589, A59
- Mushotzky, R. F., Cowie, L. L., Barger, A. J., & Arnaud, K. A. 2000, *Nature*, 404, 459
- Nardini, E. & Risaliti, G. 2011, *MNRAS*, 415, 619
- Neškova, M., Ivezić, Ž., & Elitzur, M. 2002, *ApJ*, 570, L9
- Neškova, M., Sirocky, M. M., Nikutta, R., Ivezić, Ž., & Elitzur, M. 2008, *ApJ*, 685, 160
- Osorio-Clavijo, N., González-Martín, O., Sánchez, S. F., et al. 2022, *MNRAS*, 510, 5102
- Paltani, S. & Ricci, C. 2017, *A&A*, 607, A31
- Panagiotou, C. & Walter, R. 2019, *A&A*, 626, A40
- Pouliasis, E., Mountrichas, G., Georgantopoulos, I., et al. 2020, *MNRAS*, 495, 1853
- Revnitsev, M., Gilfanov, M., Sunyaev, R., Jahoda, K., & Markwardt, C. 2003, *A&A*, 411, 329
- Ricci, C., Trakhtenbrot, B., Koss, M. J., et al. 2017, *ApJS*, 233, 17
- Ricci, C., Ueda, Y., Koss, M. J., et al. 2015, *ApJ*, 815, L13
- Satyapal, S., Abel, N. P., & Secrest, N. J. 2018, *ApJ*, 858, 38
- Sazonov, S., Churazov, E., & Krivonos, R. 2015, *MNRAS*, 454, 1202
- Sengupta, D., Marchesi, S., Vignali, C., et al. 2023, *A&A*, 676, A103
- Silver, R., Torres-Albà, N., Zhao, X., et al. 2022, *ApJ*, 940, 148
- Stern, D. 2015, *ApJ*, 807, 129
- Tanimoto, A., Ueda, Y., Oda, H., Yamada, S., & Ricci, C. 2022, *ApJS*, 260, 30
- Torres-Albà, N., Marchesi, S., Zhao, X., et al. 2021, *ApJ*, 922, 252
- Treister, E., Urry, C. M., & Virani, S. 2009, *ApJ*, 696, 110
- Tristram, K. R. W., Meisenheimer, K., Jaffe, W., et al. 2007, *A&A*, 474, 837
- Ueda, Y., Akiyama, M., Hasinger, G., Miyaji, T., & Watson, M. G. 2014, *ApJ*, 786, 104
- Ueda, Y., Akiyama, M., Ohta, K., & Miyaji, T. 2003, *ApJ*, 598, 886
- Vasudevan, R. V., Mushotzky, R. F., & Gandhi, P. 2013, *ApJ*, 770, L37
- Yamada, S., Ueda, Y., Herrera-Endoqui, M., et al. 2023, *ApJS*, 265, 37
- Yamada, S., Ueda, Y., Tanimoto, A., et al. 2021, *ApJS*, 257, 61
- Zhao, X., Marchesi, S., Ajello, M., Baloković, M., & Fischer, T. 2020, *ApJ*, 894, 71
- Zhao, X., Marchesi, S., Ajello, M., et al. 2021, *A&A*, 650, A57

Table 6. Flux and Luminosity of the sources fitted with the simple model

Source name	Intrinsic flux $\times 10^{-13}$ ergs s $^{-1}$ cm $^{-2}$				Intrinsic luminosity $\times 10^{42}$ ergs s $^{-1}$			
	$F_{0.5-2}^{\text{APEC}}$	$F_{0.5-2}^{\text{PL}}$	F_{2-10}^{PL}	F_{10-80}^{PL}	$L_{0.5-2}^{\text{APEC}}$	$L_{0.5-2}^{\text{PL}}$	L_{2-10}^{PL}	L_{10-80}^{PL}
2MASXJ01500266-0725482	-	8.38	7.90	2.01	-	0.585	0.554	0.145
NGC3094	0.25	0.48	0.63	0.94	0.004	0.007	0.009	0.013
UGC04145	0.37	0.44	0.26	-	0.019	0.022	0.014	-

Table 7. Flux and Luminosity: RXTORUS model.

Source name	Intrinsic flux $\times 10^{-13}$ ergs s $^{-1}$ cm $^{-2}$				Intrinsic luminosity $\times 10^{42}$ ergs s $^{-1}$			
	$F_{0.5-2}^{\text{APEC}}$	$F_{0.5-2}^{\text{PL,soft}}$	$F_{2-10}^{\text{RXTORUS}}$	$F_{10-80}^{\text{RXTORUS}}$	$L_{0.5-2}^{\text{APEC}}$	$L_{0.5-2}^{\text{PL,soft}}$	$L_{2-10}^{\text{RXTORUS}}$	$L_{10-80}^{\text{RXTORUS}}$
ESO420-013	0.83	1.64	255.75	17.28	3.050	7.51	25.08	1.88
ESO018-G009	2.62	-	2.71	0.76	0.017	-	0.176	0.051
UGC01214	0.62	3.16	123.61	34.7	0.020	0.102	8.04	12.09
2MASXJ04405494-0822221	0.10	-	150.31	53.88	0.005	-	7.56	13.12
CGCG074-129	-	11.71	14.14	-	-	0.009	0.81	-
2MASXJ04524451-0312571	0.05	0.27	6.79	-	0.003	0.015	0.37	-
IC4769	0.14	0.25	888.55	-	0.007	0.013	44.86	-
IC4995	0.29	0.60	214.89	56.02	0.017	0.039	13.17	3.55
NGC5990	0.35	0.57	2.96	-	0.011	0.019	0.10	-

Appendix A: The sample

Table A.1. Log of our sample

Name (I)	class (II)	Ra (III)	Dec (IV)	z (V)	logL(W3) (VI)	logL _{nuc} (VII)	L _{2-10 keV} (VIII)	NH _{los} (IX)	Ref. (X)
2MASXJ00253292+6821442*	Sy2	6.387	68.3623	0.012	42.86	42.62	43.16	23.98	1
NGC0262*	Sy2	12.1964	31.957	0.015	43.62	43.45	43.47	23.12	1
NGC0424*	Sy2	17.8651	-38.0835	0.012	43.82	43.78	42.62	24.4	2
NGC0454NED02*	Sy2	18.6039	-55.3971	0.012	43.04	43.08	42.2	23.3	1
NGC0449	Sy2	19.0302	33.0896	0.016	43.42	43.23	41.89	24.05	3
NGC0526A*	Sy2	20.9766	-35.0655	0.019	43.5	43.71	43.29	22.01	1
UGC01032*	Sy1	21.8856	19.1788	0.017	43.29	43.1	42.73	20.61	1
NGC0660	Sy2	25.76	13.6451	0.003	42.84	42.43	41.00	>23.00	4
UGC01214	Sy2	25.9908	2.3499	0.017	43.67	43.58	42.90	>24.7	This work
2MASXJ01500266-0725482	Sy2	27.5112	-7.4301	0.018	43.52	43.35	41.74	21.56	This work
NGC0788*	Sy2	30.2769	-6.8155	0.014	43.21	43.17	43.05	23.82	1
MRK1044*	Sy1	37.523	-8.9981	0.016	43.26	43.06	42.49	20	1
MESSIER077*	Sy2	40.6696	-0.0133	0.004	44.26	43.58	43.34	>25	5
MRK1058	Sy2	42.466	34.988	0.017	43.09	42.87	-	-	-
NGC1125*	Sy2	42.9185	-16.6507	0.011	43.01	42.78	42.4	24.06	6
MCG-02-08-014*	Sy2	43.0975	-8.5104	0.017	42.88	42.87	42.86	23.03	1
UGC02456	Sy2	44.9941	36.8206	0.012	43.55	43.38	42.08	23.98	7
NGC1194*	Sy2	45.9546	-1.1037	0.014	43.4	43.49	42.78	24.15	8
NGC1275*	Sy2	49.9507	41.5117	0.018	44.16	44.23	43.99	21.68	1
NGC1320	Sy2	51.2029	-3.0423	0.009	43.13	42.91	42.85	24.6	14
ESO116-G018	Sy2	51.221	-60.7384	0.018	43.57	43.41	43.23	24.41	12
NGC1365*	Sy1	53.4016	-36.1404	0.006	43.28	42.53	42.07	22.21	1
NGC1386	Sy1	54.1924	-35.9994	0.003	42.55	42.37	41.90	24.7	8
ESO548-G081*	Sy1	55.5153	-21.2443	0.014	43.21	43.04	43.03	20	1
ESO420-G013	Sy2	63.457	-32.007	0.012	43.62	43.21	43.43	>24.65	This work
2MASXJ04405494-0822221	Sy2	70.229	-8.3728	0.015	43.76	43.61	42.88	>24.47	This work
UGC03157*	Sy2	71.6236	18.4609	0.015	43.26	43.06	42.88	23.78	1
2MASXJ04524451-0312571	Sy2	73.1853	-3.2159	0.016	43.28	43.08	41.57	>23.6	This work
ESO033-G002*	Sy2	73.9957	-75.5412	0.018	43.60	43.54	42.16	22.51	1
GALEXASJ051045.55+162958.9*	Sy1	77.6896	16.4989	0.018	43.7	43.55	43.55	21.8	1
2MFGC04298*	Sy2	79.0947	19.4531	0.019	43.04	42.81	42.45	22.9	1
ESO362-G018*	Sy2	79.8992	-32.6576	0.013	43.22	43.17	42.99	20	1
NGC2110*	Sy2	88.0474	-7.4562	0.008	43.16	43.08	42.75	22.94	1
UGC03426*	Sy2	93.9015	71.0375	0.014	42.99	43.69	44.04	23.9	9
UGC03478*	Sy1	98.1965	63.6737	0.013	42.99	42.76	42.46	21.18	1
NGC2273	Sy2	102.5361	60.8458	0.006	43.01	42.78	43.11	>24.85	8
IC0450*	Sy1	103.0511	74.4271	0.019	43.76	43.62	43.12	20.76	1
UGC03752*	Sy2	108.5161	35.2793	0.016	43.56	43.39	42.77	24.02	9
2MASXJ07170726-3254197	AGN(?)	109.2802	-32.9054	0.008	42.5	42.22	-	-	-
CGCG147-020*	Sy2	111.4057	29.9541	0.019	43.4	43.08	43.32	23.86	1
UGC03995B*	Sy2	116.038	29.2474	0.016	43.38	43.19	42.47	23.92	1

Table A.1. continued.

Name (I)	class (II)	Ra (III)	Dec (IV)	z (V)	logL(W3) (VI)	logL _{nuc} (VII)	L _{2-10 keV} (VIII)	N _H ^{los} (IX)	Ref. (X)
IC2207 ^s	Sy2	117.462	33.9623	0.016	42.83	42.41	42.23	20	This work
UGC04145	Sy2	119.9172	15.3868	0.016	43.53	43.36	40.15	20	This work
PhoenixGalaxy*	Sy2	121.0244	5.1139	0.013	43.7	43.55	43.16	23.4	1
MCG-02-22-003 ^s	Sy2	125.3898	-13.3511	0.014	42.76	42.51	42.63	23.86	This work
ESO018-G009	Sy2	126.0329	-77.7826	0.018	43.43	43.25	41.23	23.49	This work
NGC2623	LINER	129.6003	25.7546	0.018	43.58	43.55	40.9	22.78	10
ARP007	Sy1	132.5843	-16.5795	0.019	43.14	42.78	-	-	-
MCG-01-24-012*	Sy2	140.1927	-8.0561	0.02	43.34	43.41	43.27	22.81	1
ESO434-G040*	Sy2	146.9173	-30.9487	0.008	43.45	43.48	43.23	22.18	1
MRK1239	Sy1	148.0796	-1.6121	0.02	44.15	44.12	42.93	23.54	11
NGC3094	AGN(?)	150.3581	15.7701	0.008	43.5	43.66	39.95	20	This work
CGCG064-055	Sy2	151.4633	12.9613	0.009	42.74	42.48	-	-	-
NGC3227*	Sy1	155.8774	19.8651	0.004	42.83	42.41	42.28	20.95	1
ESO317-G041*	Sy2	157.8463	-42.0606	0.019	43.6	43.31	42.5	24.31	6
NGC3281*	Sy2	157.967	-34.8537	0.011	43.67	43.52	42.98	24.3	12
NGC3516*	Sy1	166.6979	72.5686	0.009	43.4	43.22	42.98	20	1
IRAS11215-2806	Sy2	171.0114	-28.3877	0.014	43.21	43	-	-	-
NGC3783*	Sy1	174.7573	-37.7387	0.01	43.67	43.67	43.55	20.49	1
NGC4051*	Sy1	180.7901	44.5313	0.002	42.41	42.39	41.59	20	1
NGC4253*	Sy1	184.6105	29.8129	0.013	43.5	43.33	42.73	20.32	1
NGC4388*	Sy2	186.4448	12.6621	0.008	42.66	42.26	42.45	23.52	1
NGC4507*	Sy2	188.9026	-39.9093	0.012	43.67	43.71	43.54	23.95	1
NGC4593*	Sy1	189.9143	-5.3443	0.009	42.93	42.84	42.64	20	1
IC3639	Sy2	190.2202	-36.7559	0.011	43.52	43.44	43.4	24.56	13
NGC4628	Sy2	190.6053	-6.971	0.009	43.12	42.9	-	-	-
ESO323-G077*	Sy2	196.6089	-40.4147	0.015	43.86	43.67	42.91	22.81	1
NGC4968	Sy2	196.7749	-23.677	0.01	43.24	43.03	42.88	24.3	15
MCG-03-34-064*	Sy2	200.6019	-16.7285	0.017	44.13	43.96	43.46	24.13	20
NGC5135	Sy2	201.4336	-29.8337	0.014	43.77	43.17	43.3	24.78	10
ESO383-G018*	Sy2	203.3588	-34.0148	0.013	43.43	43.12	42.81	23.31	1
ESO383-G035*	Sy1	203.9738	-34.2955	0.008	43.07	43.06	42.75	20.85	1
2MASSJ13473599-6037037*	Sy2	206.8998	-60.6177	0.013	43.43	43.25	43.28	22.9	1
IC4329A*	Sy1	207.3303	-30.3094	0.016	44.21	44.26	43.87	21.52	1
2MASXJ13512953-1813468*	Sy1	207.8729	-18.2297	0.012	42.34	42.03	42.62	20.18	1
NGC5347	Sy2	208.3243	33.4908	0.008	42.54	42.57	42.16	>24.35	18
CGCG074-129	Sy2	212.6723	13.558	0.016	43.32	42.91	41.91	23.83	This work
CircinusGalaxy*	Sy2	213.2915	-65.3392	0.001	43.38	42.64	42.53	24.8	19
NGC5506*	Sy2	213.3121	-3.2076	0.006	43.3	43.2	42.93	22.44	1
NGC5548*	Sy1	214.4981	25.1368	0.017	43.52	43.32	43.15	20.69	1
NGC5610*	Sy2	216.0956	24.6141	0.017	43.38	43.06	42.72	22.56	1
2MASXJ14320869-2704324	Sy1	218.0363	-27.0756	0.014	42.84	42.59	-	-	-
WKK4438*	Sy1	223.8225	-51.5708	0.016	43.26	43.06	42.77	20.92	1
IC4518A*	Sy2	224.4216	-43.1321	0.016	43.6	43.5	42.67	23.36	1

Table A.1. continued.

Name (I)	class (II)	Ra (III)	Dec (IV)	z (V)	logL(W3) (VI)	logL _{nuc} (VII)	L _{2-10 keV} (VIII)	N _H ^{los} (IX)	Ref. (X)
NGC5861	Sy2	227.317	-11.3217	0.006	42.55	42.08	-	-	-
NGC5990	Sy2	236.5682	2.4154	0.012	43.58	43.29	41.00	23.43	This work
IRAS15514-3729 ^s	Sy2	238.6948	-37.6387	0.019	43.18	42.82	42.38	22.78	This work
WKK6092*	Sy1	242.9642	-60.6319	0.016	42.88	42.64	42.45	20	1
ESO138-G001*	Sy2	252.8339	-59.2348	0.009	43.57	43.58	41.56	23.6	17
ESO044-G007	Sy2	258.98	-73.3421	0.017	42.66	42.4	-	-	-
NGC6300*	Sy2	259.2478	-62.8206	0.004	42.36	42.23	41.64	23.3	1
ESO139-G012*	Sy2	264.4128	-59.9407	0.017	43.07	42.85	42.65	20	1
IC4709*	Sy2	276.0808	-56.3692	0.017	43.14	42.92	43.07	23.15	1
ESO103-G035*	Sy2	279.5848	-65.4276	0.013	43.79	43.71	43.41	23.28	1
ESO140-G043*	Sy1	281.2249	-62.3648	0.014	43.64	43.67	43.13	20	1
IC4769	Sy2	281.9335	-63.157	0.015	43.45	43.26	43.65	24.56	This work
ESO281-G038 ^s	Sy1	284.0874	-43.1469	0.017	42.98	42.75	42.63	23.34	This work
UGC11397*	Sy2	285.9548	33.8447	0.015	42.88	42.63	42.63	22.87	1
2MASXJ19373299-0613046*	Sy2	294.3875	-6.218	0.01	43.39	43.2	42.78	20.85	1
NGC6860*	Sy2	302.1954	-61.1002	0.015	43.56	43.46	43.16	21.08	1
2MASXJ20183871+4041003*	Sy2	304.6613	40.6834	0.014	43.07	42.85	42.57	22.78	1
IC4995	Sy2	304.9957	-52.622	0.016	43.25	43.05	43.11	>24.68	16, This work
MCG+04-48-002*	Sy2	307.1461	25.7333	0.014	43.62	43.45	43.16	23.86	1
ESO234-G050*	Sy2	308.9912	-50.1923	0.009	42.52	42.04	41.62	23.08	1
IC5063*	Sy2	313.0098	-57.0688	0.011	43.85	43.8	43.1	23.56	1
2MASXJ21025564+6336248	AGN(?)	315.7318	63.6069	0.011	42.59	41.66	-	-	-
IC1368	Sy2	318.5525	2.178	0.013	43.06	42.83	-	-	-
IRAS21262+5643*	Sy1	321.9391	56.943	0.014	43.51	43.33	43.1	20	1
NGC7172*	Sy2	330.5079	-31.8697	0.009	42.98	42.8	42.67	22.91	1
NGC7469*	Sy1	345.8151	8.874	0.016	44.23	43.89	43.22	20.53	1
NGC7479*	Sy2	346.236	12.3229	0.008	43.08	43.2	41.89	24.76	12
NGC7582*	Sy2	349.5979	-42.3706	0.005	43.3	42.81	43.48	24.23	12
IC1490 ^s	Sy1	359.7947	-4.127	0.019	43.3	43.11	42.51	23.3	This work

Notes: (I) Source name in (Asmus et al. 2020). (II) Optical classification from SIMBAD or NED. (III) & (IV) Optical coordinates (J2000)(V) Redshift (VI) Logarithm of W3 (12 μ m) continuum (egs/s) (VII) Logarithm of the nuclear 12 μ m luminosity of the AGN (egs/s) (VIII) Logarithm of the intrinsic 2-10 keV (egs/s) (IX) Logarithm of the column density along the line of sight (cm⁻²) (X) X-ray data reference: (1) Ricci et al. (2017), (2) Marchesi et al. (2018), (3) Guo et al. (2023), (4) Annuar et al. (2020), (5) Bauer et al. (2015), (6) Tanimoto et al. (2022), (7) Zhao et al. (2020), (8) Masini et al. (2016), (9) Marchesi et al. (2019), (10) Yamada et al. (2021), (11) Jiang et al. (2021), (12) Zhao et al. (2021), (13) Boorman et al. (2016), (14) Baloković et al. (2014), (15) LaMassa et al. (2019), (16) Osorio-Clavijo et al. (2022), (17) Sengupta et al. (2023), (18) Kammoun et al. (2019), (19) Arévalo et al. (2014), Panagiotou & Walter (2019).

* Sources detected in *Gehrels/Swift* / *Gehrels/Swift* 70 months all sky survey

^s Sources with spectra from *Gehrels/Swift* / *XRT*